Partitioned edge-function-scaled region-based active contour (p-ESRAC): Automated liver segmentation in multiphase contrast-enhanced MRI

Jihun Oh, Diego R. Martin, and Xiaoping Hu

Articles you may be interested in

Spatio-temporal texture (SpTeT) for distinguishing vulnerable from stable atherosclerotic plaque on dynamic contrast enhancement (DCE) MRI in a rabbit model
Med. Phys. **41**, 042303 (2014); 10.1118/1.4867861

3D automatic anatomy segmentation based on iterative graph-cut-ASM
Med. Phys. **38**, 4610 (2011); 10.1118/1.3602070

Computer-aided measurement of liver volumes in CT by means of geodesic active contour segmentation coupled with level-set algorithms
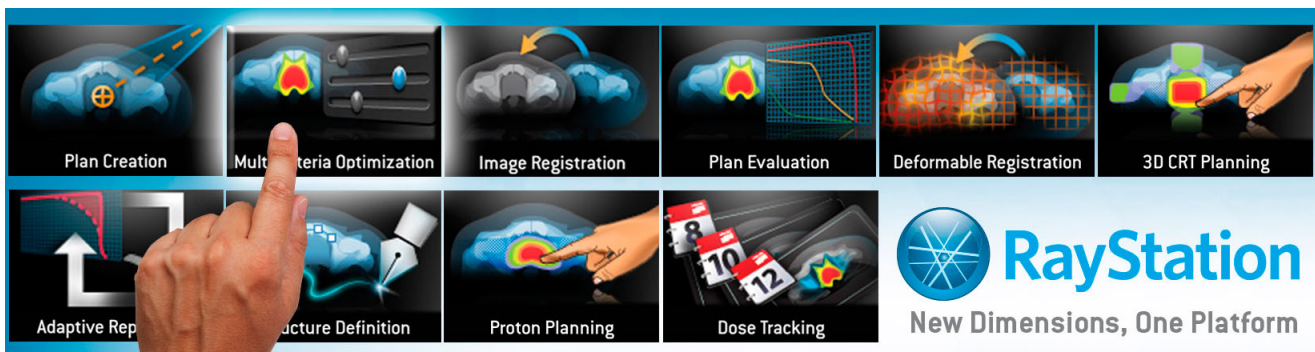Med. Phys. **37**, 2159 (2010); 10.1118/1.3395579

Computer-aided diagnosis for the classification of focal liver lesions by use of contrast-enhanced ultrasonography
Med. Phys. **35**, 1734 (2008); 10.1118/1.2900109

Quantitative evaluation of free-form deformation registration for dynamic contrast-enhanced MR mammography
Med. Phys. **34**, 1221 (2007); 10.1118/1.2712040

Partitioned edge-function-scaled region-based active contour (p-ESRAC): Automated liver segmentation in multiphase contrast-enhanced MRI

Jihun Oh
School of Electrical and Computer Engineering, Georgia Institute of Technology, Atlanta, Georgia 30332

Diego R. Martin
Department of Medical Imaging, University of Arizona, Tucson, Arizona 85724

Xiaoping Hu[a)]
Department of Biomedical Engineering, Georgia Institute of Technology and Emory University, Atlanta, Georgia 30332

Purpose: In multiphase contrast-enhanced magnetic resonance imaging (CE-MRI), liver segmentation is an important preprocessing step for the computer-aided evaluation of liver disease. However, because of the liver's irregular shape, proximity to surrounding organs, and large intensity variation, and peripheral contrast enhancement in the kidney, liver segmentation has been very challenging. This paper presents a novel hybrid active contour model and overall procedures that are specific to liver segmentation.

Methods: The authors introduced an edge-function-scaled (weighted) region-based active contour model (ESRAC) and utilization of registered, multiphase sequences to address leakage-to-kidney and oversegmentation problems. The model incorporated weighted regional information with a compactly supported edge map, computed from a combination of images obtained during arterial and delayed phases, and it was coupled with a geodesic edge term. To cope with signal-inhomogeneity on MRI, all of the axial slices were partitioned into eight sectors with an angular span of $45°$, centered on the inferior vena cava, each in the superior and inferior regions and the regional information regarding ESRAC was computed for each partition, henceforth the so-called partitioned ESRAC (p-ESRAC). Initialization of the active contour was performed by thresholding with a range of $[200, +\infty)$ and simple morphological operation during the delayed phase. At the end, to fill the holes in the segmented images caused by high gradients around the vasculature, noise, or outstanding texture features, iterative morphological operations were performed until convergence. The authors compared the segmentation accuracy of p-ESRAC to that with geodesic active contour, region-based active contour, geodesic active region, and localized region-based active contour using quantitative and visual assessments.

Results: In three-dimensional experimental studies conducted on 30 subjects (14 normal or benign cases and 16 malignant cases), compared with other active contours, p-ESRAC achieved the highest dice similarity coefficients of $93.9 \pm 1.6\%$ (normal) and $91.6 \pm 2.2\%$ (malignant), respectively. In addition, p-ESRAC resulted in the lowest false positive rates of $4.5 \pm 3.2\%$ (normal) and $7.9 \pm 3.0\%$ (malignant), demonstrating it to be the most effective in reducing oversegmentation. The partition scheme improved segmentation accuracy by $5.4 \pm 9.2\%$ (normal) and $22.2 \pm 27.6\%$ (malignant) of the true segmentation that was missed by ESRAC. Visual assessment confirmed that p-ESRAC prevented leakage of the segmentation results of the liver into the kidney.

Conclusions: A novel active-contour model was developed, allowing for accurate liver segmentation on multiphase CE-MRI, with conditions that include signal inhomogeneity and weak boundary conditions. Such a technique could be useful for applications that involve computer-aided diagnosis of liver disease. © *2014 American Association of Physicists in Medicine.* [http://dx.doi.org/10.1118/1.4867865]

1. INTRODUCTION

Magnetic resonance imaging (MRI) is among the most widely used diagnostic imaging modalities, particularly in the imaging of soft tissue organs, such as the liver. Contrast-enhanced liver MRI can be useful for numerous applications, such as organ volume analysis, contrast-uptake-time curves, and evaluation of tumors, and for the analysis of changes related to diffuse liver disease. To define the volume of interest (VOI) for further analysis, liver segmentation is a necessary preprocessing step. Segmentation in medical imaging can be divided into manual, interactive, and fully automated approaches. In

practice, interactive approaches, such as graph-cut[1] and live-wire[2] segmentation, have been popular because they allow for rapid verification and adjustment of automated techniques. However, they impose an enormous burden on users when a large amount of data must be processed. Therefore, fully automated segmentation has become a necessity, but well-developed techniques remain underdeveloped.

Liver segmentation is extremely challenging because of the proximity of the liver to its surroundings and the large intensity variations within it. The organs surrounding the liver include the kidneys, pancreas, lungs, and heart. Renal excretion of injected contrast material can lead to contrast enhancement in the kidneys, making segmentation of the liver difficult. In addition, intensity variation in the liver can arise from nonuniform static magnetic and RF fields[3] and from nonuniform uptake of the injected contrast agent.

Liver segmentation techniques for MRI remain limited. In contrast, a number of approaches have been developed for liver segmentation on computed tomography (CT) scans.[4] Shape-constrained segmentation using a statistical shape model[4–6] has shown the greatest accuracy among automatic methods, but it requires an extensive library of training shapes (100+ data sets) and landmarks (~ 2500 points) because of the broad variation in the shape of the liver. Probabilistic atlas-based methods[7,8] have been applied using combinations of statistical priors or deformation models, but they still must be improved. An approach based on region growing using a partitioned probabilistic model[9] that divides the liver into eight parts has been demonstrated to be feasible and efficient with contrast-enhanced MRI (CE-MRI), but it can result in leakage of segmentation because of lack of topological constraints and peripheral contrast enhancement in adjacent organs. Another algorithm, the graph-cut method,[1] is an interactive refinement process that is highly user-interaction intensive.

The active contour approach, which uses level set representation, is a widely used segmentation approach. It is advantageous because the resulting contours facilitate labeling without requiring an additional process of connecting boundaries and because it allows for the merging and splitting of multiple contours. However, the inherent problem with this method is that the resulting contours are dependent on the initial selection of the contour. In addition, classic active contour methods, such as those based on edge-based geodesic active contour (GAC) and region-based active contour (RAC), which use either gradient or regional statistics, are insufficient for imperfect medical images. A unified approach to mitigating this problem is based on geodesic active regions (GAR);[10] this method extracts the boundary attraction from the geodesic active-contour framework and computes the regional attraction by maximizing the *a posteriori* frame partition probability. However, limitations of this method have arisen because, on contrast-enhanced MRI, the liver might not have a Gaussian profile that distinguishes it from the surrounding organs. Consequently, the segmented liver can contain nonliver regions, the intensity of which overlaps with that of the liver. Localized region-based active contour (LRAC) (Refs. 11 and 12) uses regional energy to treat cases in which global statistics cannot represent the foreground and background in all of the local regions. Its major problems are greater sensitivity to initialization, greater computational complexity than global region-based methods, and difficulty in determining the local radius of the window.

In this paper, we present a novel coupled active contour with the aid of multiphase characteristics, which was adapted to reduce oversegmentation in contrast-enhanced liver MRI segmentation. The partition scheme was also applied to account for heterogeneous intensity statistics in different parts of the liver. We compared its performance to that of existing active-contour models based on three-dimensional (3D) experimental studies.

2. METHODS

2.A. Edge-function-scaled region-based active contour (ESRAC)

Hybrids of boundary-based segmentation and region-based segmentation, such as GAR, incorporate the limited use of the intensity information of an image, but they are not sufficiently constrained to stop the evolution of the curve near a high gradient, seemingly an edge, in a homogeneous local region. Consequently, many tasks in medical imaging, including liver segmentation on CE-MRI, suffer from leakage of the curve. To prevent this leakage, we propose that the regional information used in the active contour be weighted by the edge function. An edge-scaled (weighted) regional term is defined as

$$R = \int_{C_{\text{in}}} g(I(x, y))|I(x, y) - c_1|^2 dxdy$$
$$+ \int_{C_{\text{out}}} g(I(x, y))|I(x, y) - c_2|^2 dxdy, \qquad (1)$$

where C_{in} and C_{out} denote the interior region and the exterior region of the contour in image I, and c_1 and c_2 are the average intensities in each region, updated for each iteration. $g(I(x, y))$ is an edge function that is a positive and decreasing function of the gradient of the Gaussian-smoothed image I. Here, the weightings for the foreground and the background are identical. This regional term is coupled with a geodesic edge term, defined as the geodesic length of a curve in Riemannian space; thus, the energy functional for the ESRAC model becomes

$$\text{ESRAC} = \alpha R + (1 - \alpha) \int_0^L g(|\nabla I(C(q))|) ds$$
$$+ \nu \int_{C_{\text{in}}} dxdy, \qquad (2)$$

where α controls the balance between the regional term and the edge term, and $ds = |C'(q)|d$. $C(q) : [0, 1] \rightarrow \mathbf{R}^2$ is the parameterized, enclosed planar curve. The last regularizing term is intended to make the curve more regular, and it is associated with the area of the region inside the curve. The term ν controls its weighting. The associated Euler-Lagrange

equation for level set ϕ yields

$$\frac{\partial \phi}{\partial t} = |\nabla \phi| \left[\underbrace{\alpha(-g(I)(I - c_1)^2 + g(I)(I - c_2)^2)}_{\text{region−based term}} \right.$$

$$\left. + \underbrace{(1 - \alpha)\left(g(I)\kappa + \nabla g(I) \cdot \frac{\nabla \phi}{|\nabla \phi|}\right) - \nu}_{\text{edge−based term}} \right], \quad (3)$$

where κ is a curvature, defined as div$(\frac{\nabla \phi}{|\nabla \phi|})$. To date, the edge functions have been monotonically decreasing and asymptotically approaching zero as the gradient approaches infinity. However, because of the open bound in the interval $[0, +\infty)$, setting up the gradient threshold numerically to force the edge function to zero has been controversial. Additionally, the L^2 norm of the gradient is anisotropic, despite the intensity change being equivalent in all directions. Therefore, we introduce a novel compactly supported edge function with a L^∞ norm, given by

$$g(I(x, y)) = (1 - \lambda|\nabla G_\sigma * I(x, y)|_\infty^2)_+^2, \quad (4)$$

where $f = (1 - r)_+^2$ indicates that the function f is zero if r is greater than 1. This function is continuous and differentiable at $r = 1$, so it belongs to class C^1. The threshold λ is the inverse of the lowest squared L^∞ norm that makes Eq. (4) equal to zero, or $\lambda = \frac{1}{|\nabla G_T|_\infty^2}$.

Table I lists the different characteristics of active contour models, using every possible combination in terms of edge and regional significant differences. In particular, in separable regions with above-threshold gradient magnitudes but statistically insignificant regional differences and vice versa, the existing hybrid methods (GAR or LRAC) cannot ensure that the contour stops unless the sum of the regional and edge energies becomes zero. In contrast, ESRAC can stop at the boundary because the regional term is weighted with the edge function of zero value, which forces both the regional energy and the edge energy to zero. Additionally, in the opposite case, with a small gradient but statistically significant regional difference, the evolution of ESRAC can be stopped by the minimization of the regional energy, which contributes more to the total energy than to the edge energy. It can occur that an edge indicating some of the features (e.g., vasculature) in the target may not be included in the segment by ESRAC. However, if it is geometrically enclosed or semienclosed by the curve, the region will be included by the postmorphological operation.

TABLE I. Propagation states of various active contours—GAC, CVRAC, GAR, LRAC, and ESRAC—depending on the existence of the edge and regional significant differences.

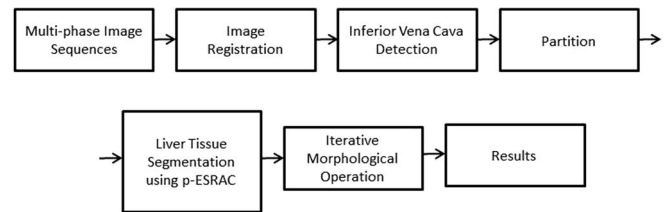|	GAC	CVRAC	GAR/LRAC	ESRAC
Edge: Yes; regions: Yes	Stopped	Stopped	Stopped	Stopped
Edge: Yes; regions: No	Stopped	Moving	Either	Stopped
Edge: No; regions: Yes	Moving	Stopped	Either	Stopped
Edge: No; regions: No	Moving	Moving	Moving	Moving

FIG. 1. Liver segmentation steps.

2.B. Application to multiphase contrast-enhanced liver MRI

As shown in Fig. 1, our liver segmentation consisted of five steps: (1) image registration of all of the phases to correct for motion artifacts; (2) inferior vena cava detection to find the origin of the partition; (3) partitioning to separate the entire image volume into multiple regions; (4) active contour to segment the liver tissue; and (5) an iterative morphological operation to fill the elongated holes and smooth the surface.

2.C. Multiphase image registration

For motion correction of the liver on multiphase images, translation-only registration corrects for most rigid-body motion. We searched for the translational direction for which the normalized cross-correlation over the rectangular mask containing the liver would be maximized. Under the assumption of affine and local changes in contrast, the bidirectional local correlation coefficient Demons algorithm,[13] which is a variation of the original Demons algorithm, was used to correct for the remaining nonrigid tissue motion. The velocity field for each iteration was computed, and the iteration stopped when the sum of the local correlation coefficients over the mask no longer improved. Because the numerical computation was simple and highly parallelizable, it could be implemented on a graphical processing unit (GPU) and could achieve a subminute runtime with a high speed-up factor. In simulations using an artificially deformed phantom image, the average displacement error was shown to be 0.34 mm (subvoxel size).

2.D. Liver partitioning

The signal quality of contrast-enhanced liver MRI can be affected by inhomogeneities caused by scanner imperfection and localized contrast uptake. To improve intensity-based segmentation, bias field correction is necessary. One approach is to estimate the bias field directly in a parametric[14] or nonparametric[15] manner. However, this approach assumes that the image is composed of pixels assigned to a small number of categories, so it is more appropriate for brain or breast MRI than for abdominal MRI, in which multiple structures are present. The alternative is to divide the image volume into multiple partitions in a predefined pattern and to compute the foreground and background regional statistics for each partition separately in the segmentation framework. In this research, each axial plane was divided into multiple partitions with the angular span of 45°, centered from the inferior vena
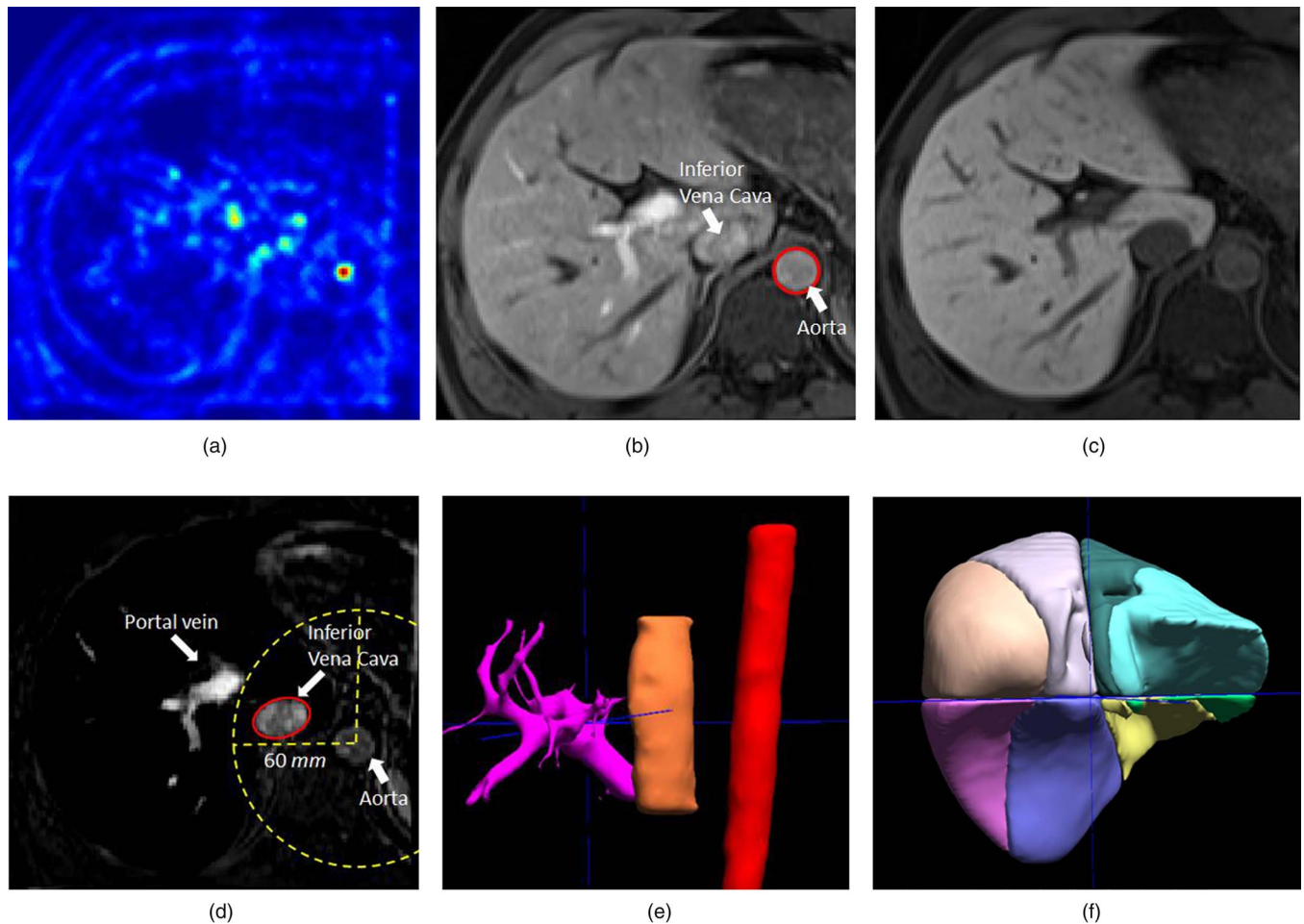
FIG. 2. Partition of the liver: (a) and (b) An accumulation map of the circular Hough transform for detecting the aorta in the arterial phase; (c) the delayed phase; (d) inferior vena cava detection (ellipse) within a certain range (dashed circle) of distance from the aorta in the subtraction of the delayed phase from the arterial phase (axial view); (e) a 3D rendering lateral view of the portal vein, inferior vena cava, and aorta from left to right; (f) a lateral view of liver partitions represented with labels (angular distance = 45°).

cava. In Fig. 2, to determine the center of the inferior vena cava, a circular Hough transform[16] first detected the circular shape of the abdominal aorta within a specific diameter range (14–24 mm) on each axial plane during the arterial phase. Then, the postcontrast enhanced delayed phase image was subtracted from the earlier arterial phase image, which had positive intensities only in the inferior vena cava and the portal vein inside the liver region. A search was undertaken for the inferior vena cava within 60 mm of the aorta. On each axial plane, the center of the inferior vena cava was determined using the ellipse detection method,[17] with the range of the major axis of the ellipse set to between 5 and 30 mm and the accumulator points weighted by the grayscale intensity. Additionally, the portal vein was identified via thresholding (greater than 100) and by searching for the largest 3D connected region located in the region to the left of the inferior vena cava. The image volume was bisected into superior and inferior regions by the axial plane passing through the centroid of the portal vein segment. This radial pattern allowed each partition to have the liver (foreground) and nonliver (background) regions simultaneously used for p-ESRAC, and

it approximated the radial vascular network of the hepatic vein.[18]

To apply these partitions in the ESRAC model, we constructed a label array $L(x, y)$ that consisted of integer elements 1 to M to represent M exclusive partitions. A mask $T(L(x, y), k)$, corresponding to the kth partition, is given by

$$T(L(x, y), k) = \begin{cases} 1, & \text{if } L(x, y) = k; \\ 0, & \text{otherwise,} \end{cases} \qquad (5)$$

Partitioned regional energy term (c_1^k, c_2^k, C)

$$= \sum_{k=1}^{M} \left[\int_{C_{in}} T(L(x, y), k) g(I(x, y)) \right.$$

$$\times |I(x, y) - c_1^k|^2 dx dy + \int_{C_{out}} T(L(x, y), k) g(I(x, y))$$

$$\left. \times |I(x, y) - c_2^k|^2 dx dy \right], \qquad (6)$$
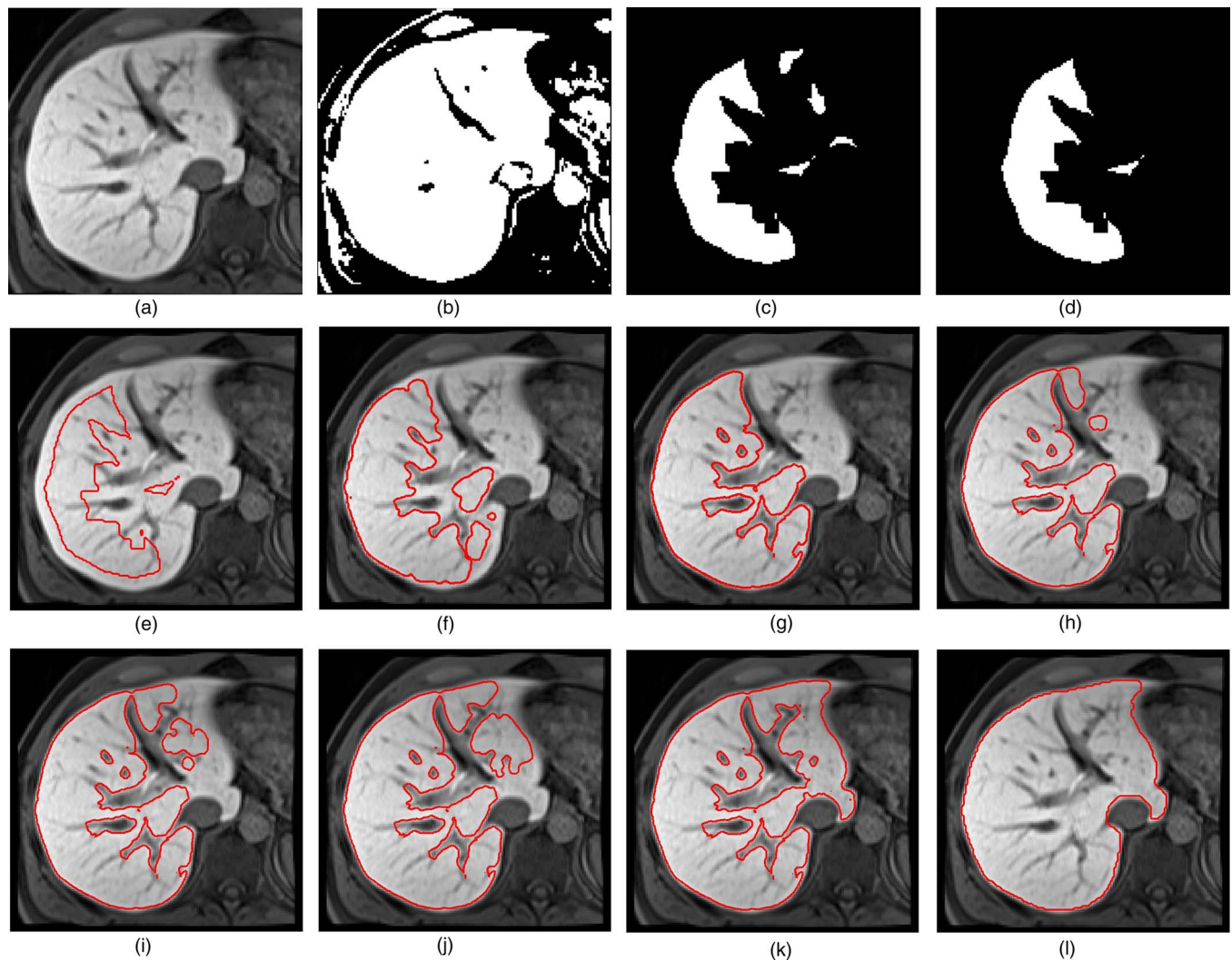
FIG. 3. Initialization, contour evolution, and iterative morphological operation: (a) original delayed-phase image; (b) thresholding above the intensity of 200; (c) 3D erosion (several neighboring regions are not 3D-connected); (d) the selection of the largest connected 3D region; (e)–(k) resulting contours at 1, 50, 150, 350, 500, 600, and 1000 iterations; (l) iterative morphological operations (filling and closing).

where c_1^k and c_2^k denote the average intensities inside and outside the contour in the kth partition, respectively. The associated level set is given by

$$\frac{\partial \phi}{\partial t} = |\nabla \phi| \left\{ \alpha \sum_{k=1}^{M} T(L,k) \left[g(I)\left(I - c_1^k\right)^2 + g(I)\left(I - c_2^k\right)^2 \right] \right.$$

$$\left. + (1-\alpha)\left(g(I)\kappa + \nabla g(I) \cdot \frac{\nabla \phi}{|\nabla \phi|} \right) - \nu \right\}. \qquad (7)$$

2.E. Liver tissue segmentation using p-ESRAC

To initialize a seed contour, as shown in Figs. 3(a)–3(d), thresholding with a range of $[200, +\infty)$ was applied to the delayed-phase image. Subsequently, to remove isolated segments and unnecessary connections from surrounding objects, we performed four iterations of 3D erosion using a spherical structure with a five-voxel radius on the resultant binary image. Then, from the eroded binary mask, the largest connected 3D region with six connected neighbors was chosen as the

initial segmentation mask. To apply the level set framework of p-ESRAC, the initial mask was used for calculating the signed distance function (SDF), representing the level set, the zero (SDF = 0) of which was located between the foreground (SDF > 0) and background (SDF < 0) regions.

The intensity probability density distributions for the liver and other surroundings in normal subjects and subjects with disease are different. The contrast of the liver against the abdominal wall, pancreas, and stomach is high during the delayed phase in both cases. However, regarding contrast against the kidney, the contrast is not the same. The kidney appears most enhanced during the arterial phase and then decreases with time, while the liver remains enhanced up to the delayed phase in normal subjects. However, in cases of pathology, the uptake of the contrast agent by liver cells is absent, so the signal remains constant or decreases after the first peak during the arterial phase. Therefore, during the delayed phase, the contrast between the liver and the kidney in pathological cases is not as high as in the normal case. That the high contrast of the liver against the kidney is acquired from the arterial phase,
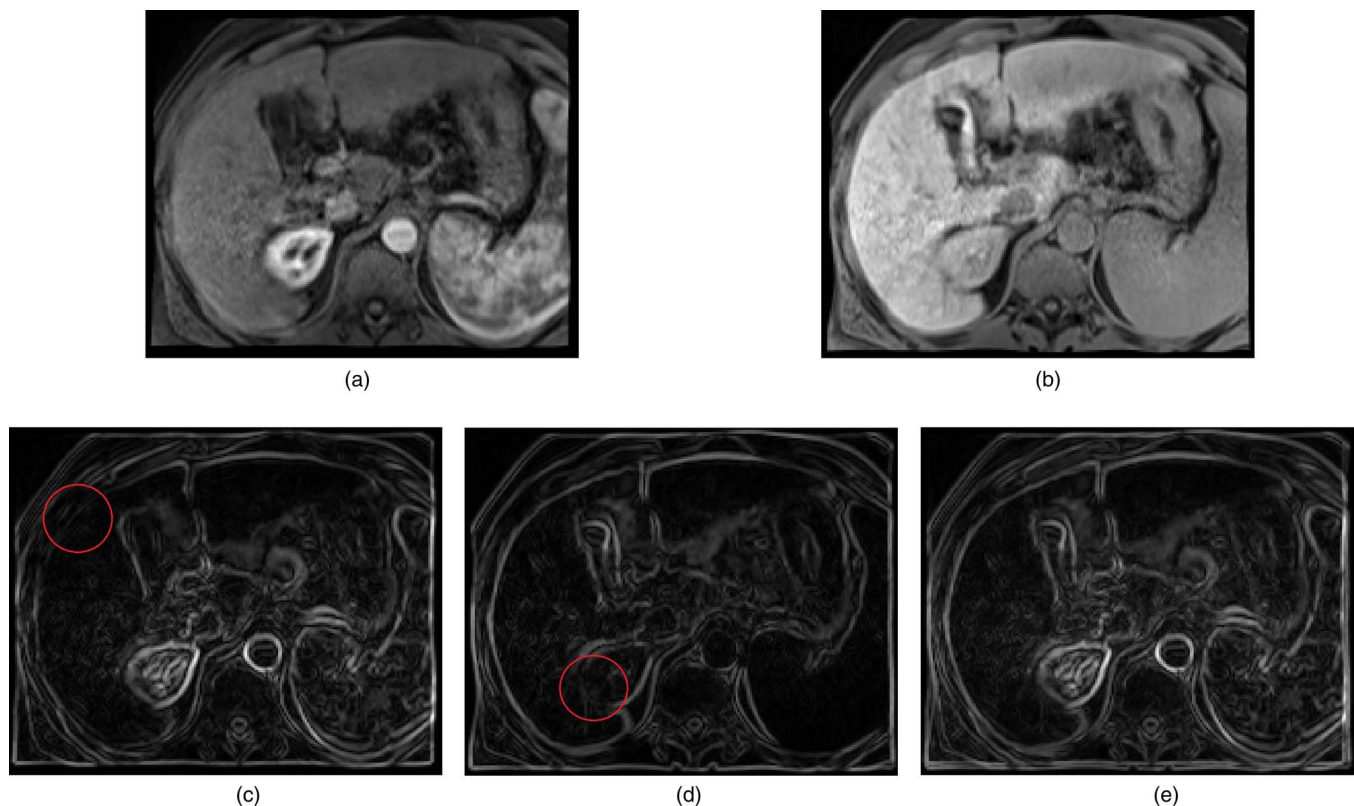
FIG. 4. Computation of the gradient: (a) motion-corrected image during the arterial phase; (b) motion-corrected image during the delayed phase; (c and d) the L^∞ norms of the gradient during the arterial and delayed phases, respectively; (e) the element-wise maxima of the L^∞ norms during the two phases. The circles indicate regions where the gradient is not sufficiently large during each phase. This combination yielded a better gradient image (e).

while the high contrast against all other surroundings, except for the kidney, is acquired from the delayed phase, helps to address this problem. To incorporate this knowledge into the ESRAC model, elementwise maxima of the L^∞ norms of the gradient are computed in the Gaussian-smoothed arterial and delayed phases, as shown in Fig. 4, while the partitioned regional statistics are computed in the delayed phase only. Prior to segmentation, resampling to the isotropic voxel size is necessary for the smooth evolution of the contour. As illustrated in Figs. 3(e)–3(k), the active contour is iteration-based, so it is repeated until the mean of the absolute difference between the current and previous level sets in the entire image domain is less than 5×10^{-4}. The maximum number of iterations was 10^3. The parameters α and ν in Eq. (7) were 0.9 and 0.02, respectively. The sigma of the Gaussian smoothing was 0.5, and the gradient threshold λ in Eq. (4) was 10^{-2}.

2.F. Iterative morphological operations

Upon completing the segmentation using the active contour described above, iterative morphological operations (IMOs) were performed to acquire the enclosed and smooth segmented volume. Intensity-based methods are prone to missing vasculature or outstanding textural features inside the liver. Furthermore, p-ESRAC responds more sensitively to the edge map than the original region-based active contours. Our solution was to first apply a filling operation to remove the elongated holes and then a closing operation, which con-

sisted of dilation followed by erosion, using a 3D morphological structuring element with a $3 \times 3 \times 3$ ball. These IMOs were repeated until the volume of nonzero voxels no longer changed, yielding a single contour curve with no holes, as illustrated in Fig. 3(l).

3. EXPERIMENTAL RESULTS

A gadolinium (Gd)-based, contrast-enhanced, T1-weighted gradient echo protocol[19] was used to image the liver in 30 human test subjects: 14 normal or benign cases diagnosed with chronic liver disease and 16 malignant cases with cirrhosis or necrosis. Additional five human subjects (three normal and two benign) were used for training and the selection of parameters. In validating the registration method, we used eight different divergence-free deformation models to derive the true deformation field and to generate the target image by adaptively deforming the reference image[13] because the true dense deformation field between two given multiphase MR images is generally unknown. In contrast, segmentation of the contrast-enhanced liver using real image data can be manually delineated by clinical experts, and it is generally regarded as ground truth. The imaging protocol consisted of three-dimensional precontrast (0 s) and postcontrast scans (20 s: arterial phase; 1 min: portal-venous phase; 20 min: delayed phase) after the administration of a gadoxetic acid (Gd-EOB-DTPA) contrast agent (Eovist; Bayer HealthCare). The contrast agent was taken up by liver

tissue, enhancing healthy liver tissue, while lesions with no or minimal hepatocyte function remained unenhanced. Note that approximately 50% of the injected contrast agent was renally excreted, whereas the other 50% was transported to the liver and then excreted via the biliary system.[20] This dual elimination yielded contrast enhancement in two organs with different patterns over time. The size of each scan was 256 × 256 × 128, the inplane resolution was 1.46 mm, and the slice thickness was 3 mm without a gap. All of the patient MRI data were obtained with hospital internal review board approval, and this study was HIPAA-compliant.

A reference volume was manually delineated by a radiologist for use as a gold standard in evaluating the performance of the segmentation. It was initiated by thresholding and was then modified by removing or adding the extra volume or by filling the gaps manually using a graphic tool. The same initial seeds were applied to the initialization of all the automated segmentations. We performed exemplary segmentation methods and quantified the segmentation accuracy using the following metrics: the dice similarity coefficient (DSC), the true-positive rate (TPR), the false-positive rate (FPR), the volumetric overlap error (VOE), and the average symmetric surface distance (ASSD) which computes the average distance of the closest voxels along the reference and segmented borders. The R^2 coefficient, which is the square of the correlation coefficient between the reference and segmented volumes, was also evaluated. Larger absolute values of DSC, TPR, and R^2 and smaller absolute values of FPR, VOE, and ASSD corresponded to greater segmentation accuracy:

Metric	Definition
DSC	$\dfrac{V_S \cap V_R}{0.5 * (V_S + V_R)}$
TPR	$\dfrac{V_S \cap V_R}{V_R}$
FPR	$\dfrac{V_S \cap V_R^c}{V_R}$
VOE	$1 - \dfrac{V_S \cap V_R}{V_S \cup V_R}$

where V_S and V_R denote the segmented and reference-volume masks, respectively, which could have values of 0 or 1.

3.A. Validation of partitioned ESRAC (p-ESRAC)

To validate the partitioning of the liver, the results with p-ESRAC were compared to those with ESRAC. The application of segmentation algorithms can result in segmentation consisting of too few (undersegmentation) or too many (oversegmentation) regions. In Fig. 5, signal inhomogeneity appears over several vulnerable regions that are susceptible to undersegmentation, particularly where the left lobe region was lower in intensity than the other regions. In the test results, a large portion of the segmented volume was similar between p-ESRAC and ESRAC. However, when using ESRAC, the vulnerable regions were not included. In contrast,
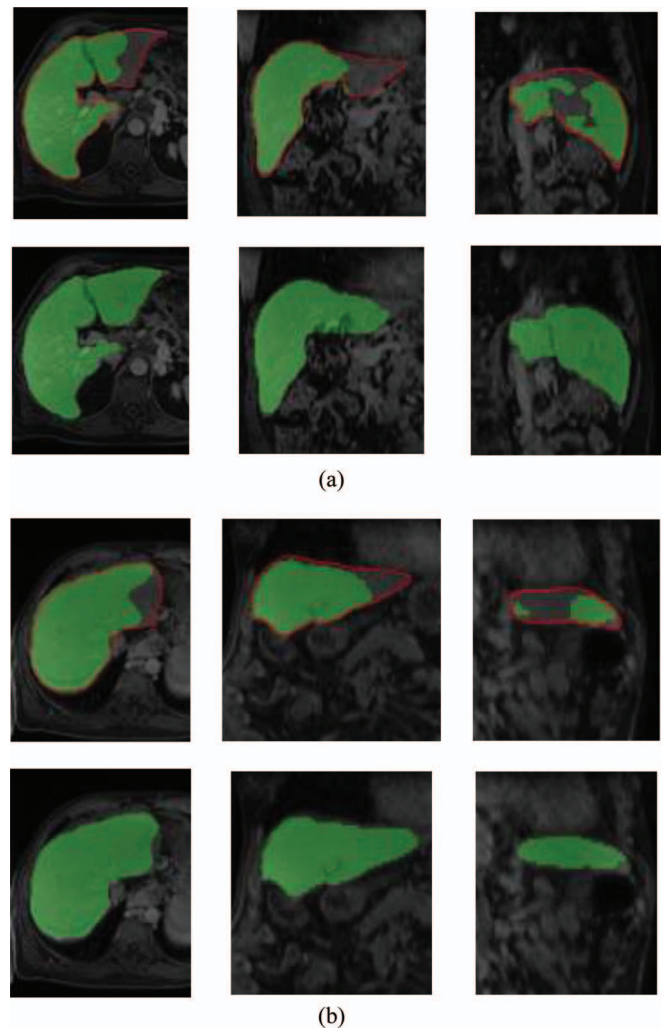

FIG. 5. Visual comparison between p-ESRAC and ESRAC. For two malignant cases (a) and (b), the first row indicates the segmentation (mask) with ESRAC with the reference (contour) superposed, while the second row indicates the segmentation with p-ESRAC on the axial (first column), coronal (second column), and sagittal (third column) planes.

the p-ESRAC segmentation, which was dictated by the local mean in the partition to which the contour segment belonged, identified a greater liver volume in the region than ESRAC segmentation.

To measure the improvement quantitatively, we introduced in Eq. (8) a segmentation improvement ratio to demonstrate the change in volume segmented by p-ESRAC relative to the volume segmented by ESRAC. The first term of the metric indicates the ratio of the true volume added by p-ESRAC to the true volume missed by ESRAC. The second term indicates the ratio of the true volume missed by p-ESRAC to the true volume segmented by ESRAC

Segmentation improvement ratio

$$= \frac{V_A^c \cap V_B \cap V_R}{V_A^c \cap V_R} - \frac{V_A \cap V_B^c \cap V_R}{V_A \cap V_R}, \qquad (8)$$

where V_A and V_B are the volume masks segmented by ESRAC and p-ESRAC, respectively, and V_R is the reference volume mask. Table II shows that the results changed as how

TABLE II. The values of the segmentation improvement ratio relative to the angular distance in partitioning. The boldface value indicates the optimal solution in a given set of tests.

Angular distance (deg)	Number of partitions	Mean ± Std (%)	
		Normal and benign	Malignant
15	48	2.44 ± 9.23	6.18 ± 10.11
30	24	4.73 ± 9.34	9.96 ± 13.10
45	**16**	**5.39 ± 9.17**	**22.19 ± 27.55**
60	12	3.74 ± 8.49	12.37 ± 14.80
90	8	2.72 ± 6.42	16.24 ± 21.91

finely the whole region was partitioned. It is obvious that p-ESRAC exhibited improved performance compared with ESRAC and that, in normal cases, the angular distance of 45° (16 partitions, eight each in the superior and inferior regions) yielded the highest segmentation improvement ratio of 5.39 ± 9.17%. In the malignant cases, the measurement with the same settings increased to 22.19 ± 27.55%. This finding demonstrates that the partition significantly improved the segmentation accuracy, especially with the angular distance of 45° showing the best numerical results. In fact, the partition configuration most closely approximated the angular spacing of the three hepatic veins, used for dividing functional liver anatomy, radially distributed in the liver.

3.B. Comparison of p-ESRAC to other techniques

To confirm that p-ESRAC is most suitable for contrast-enhanced liver MRI, we compared p-ESRAC to other intensity-based automated segmentation techniques, including GAC and Chan-Vese region-based active contour (CVRAC) methods, as well as hybrid methods of GAR and LRAC. In the cases of the methods that use regional information, they were modified to accommodate the partition scheme and are referred to as p-CVRAC and p-GAR. Note that LRAC inherently benefited from localization in a dynamic way, so it was not tested with the partition scheme. Empirically, the size of the local mask applied in LRAC was tuned to be ∼20 voxels. For all of the methods, we used an identical edge map that was extracted during the arterial and delayed phases, and regional information was obtained during the delayed phase only, as explained in Sec. 2. After segmentation, IMO was performed.

Figure 6 shows that p-CVRAC produced better results than the previous methods, substantially curbing oversegmentation, but the leakage-to-kidney problem still occurred and must be addressed. Our p-ESRAC method worked exceptionally well in most of the cases, considerably improving the oversegmentation problem. In comparison with the existing hybrid active contours in Fig. 7, p-GAR could not avoid leakage to the kidney and to a small portion of the surroundings in all three cases. LRAC prohibited leakage to the kidney in the first two cases, in which the boundary with the kidney was clear, yet it still suffered from this problem under the more difficult conditions of the third case. In addition,
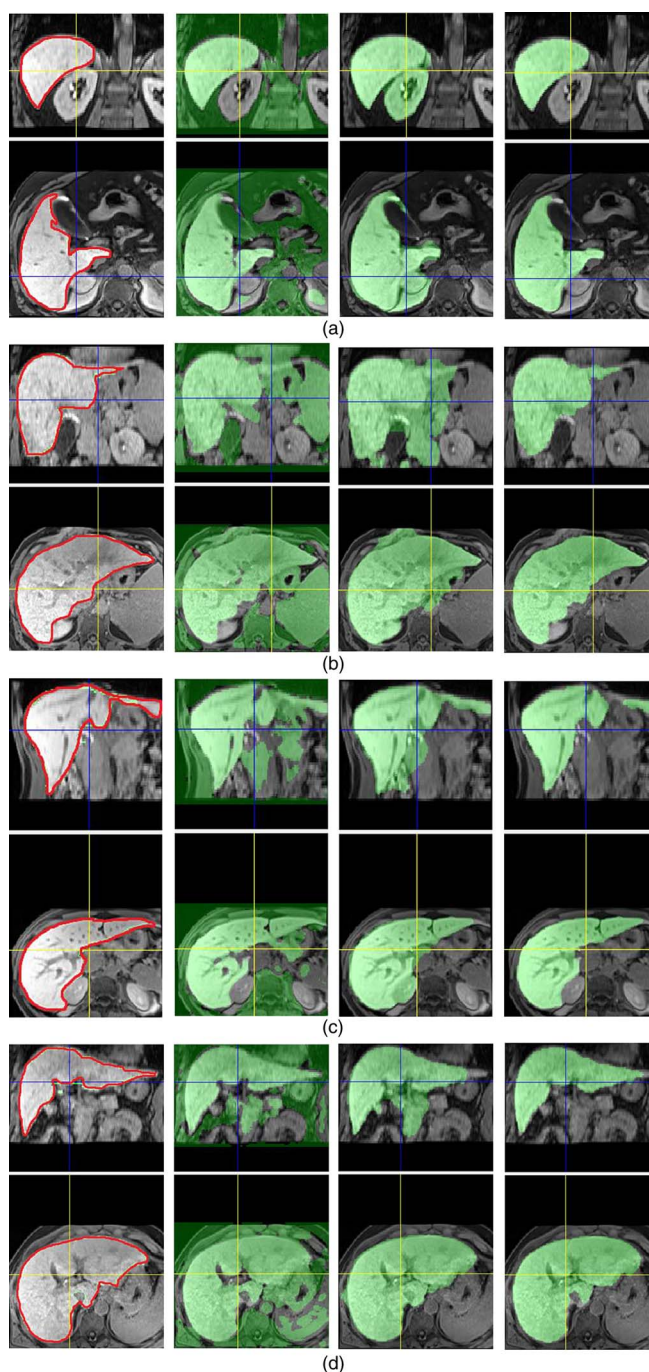

FIG. 6. Visual comparisons among the four segmentation approaches. The reference contour is inscribed on the delayed phase (first column), the segmentations (masks) with GAC (second column), p-CVRAC (third column), and p-ESRAC (fourth column) are shown for four different subjects. The results are shown on the coronal (top) and axial (bottom) planes.

it suffered from undersegmentation in the liver tissue near strong vascular structures, which could be attributed to the greater sensitivity of LRAC to local changes. In contrast, p-ESRAC outperformed all of the other methods evaluated here and yielded the most desirable results, with neither leakage nor undersegmentation. Based on the dice similarity coefficient and volumetric overlap error quantifying the overlap between the automatic and manual segmentations for the normal and benign cases in Fig. 8, p-ESRAC proved to be superior.
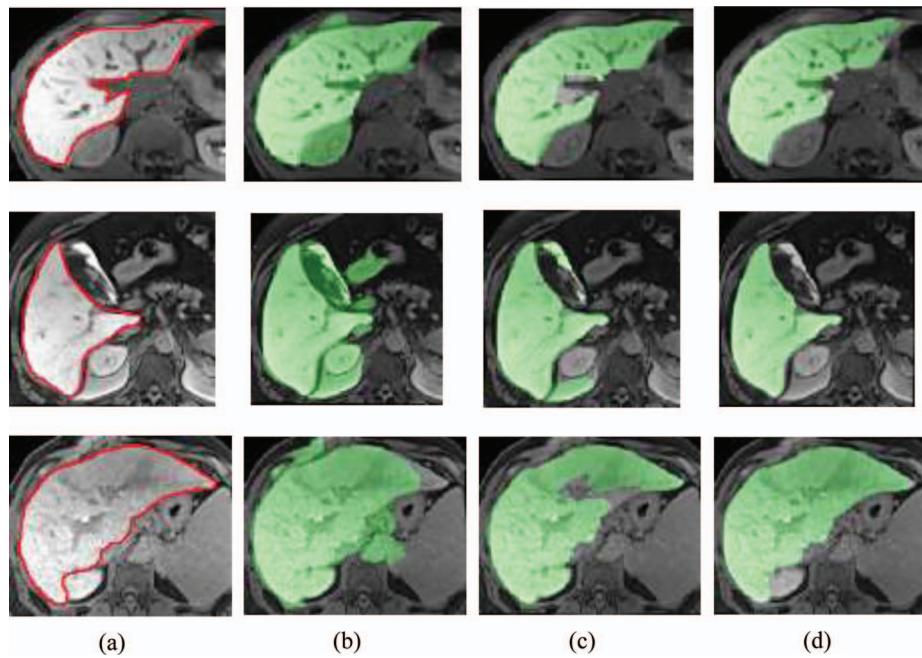
FIG. 7. Visual comparisons among hybrid active contours: (b) p-GAR, (c) LRAC, and (d) p-ESRAC. The original image and the reference contour are shown on the delayed phase in the first column (a), and the segmentation results are shown as masks.
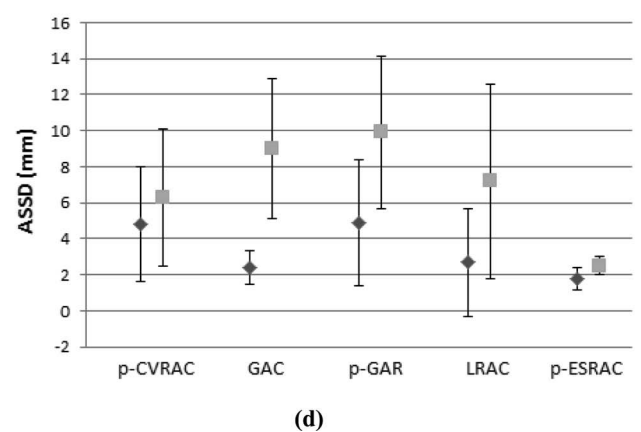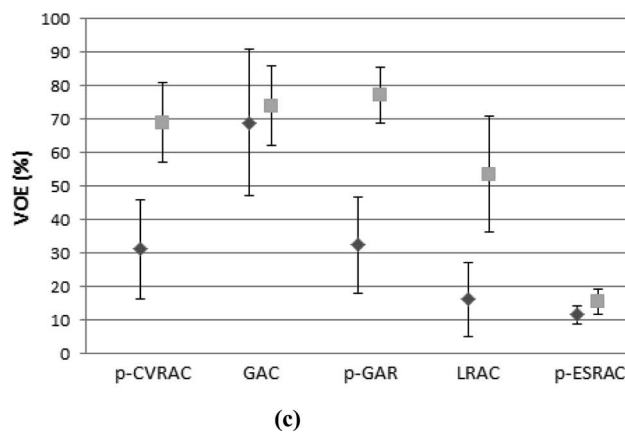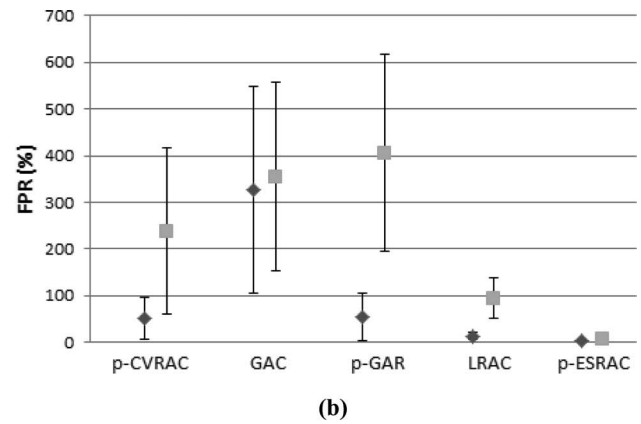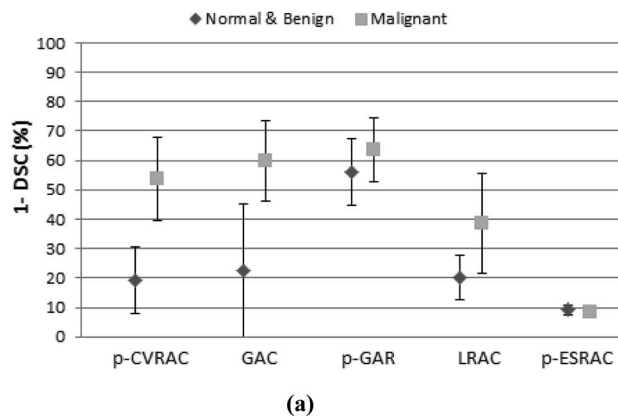

FIG. 8. Segmentation accuracy (mean and standard deviation) comparisons among intensity-based active contours tested in normal or benign cases (diamond) and malignant cases (square) in the metrics of (a) DSC, (b) FPR, (c) VOE, and (d) ASSD. Note that DSC is changed to 1-DSC for consistency with the other graphs.
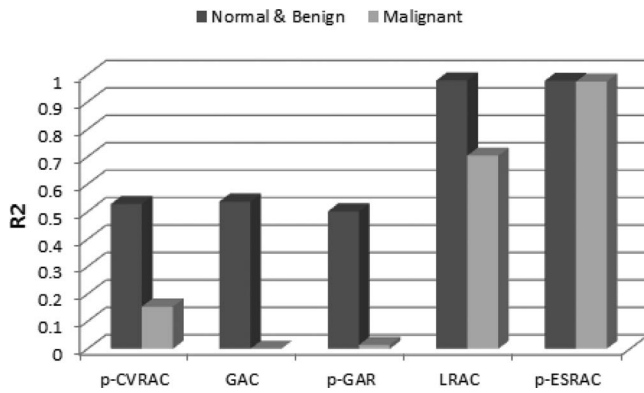
FIG. 9. Correlation between the segmented volume and the reference volume in normal-benign case and malignant case.

TABLE III. The ratio of structures excluded in segmentation, resulting from active contours, to the final volume after iterative morphological operations.

	Mean	Standard deviation
p-GAR	6.23%	0.45%
LRAC	5.91%	0.15%
p-ESRAC	11.78%	1.09%

The false-positive rate, which accounts for oversegmentation, indicated that p-ESRAC considerably decreased oversegmentation artifacts and had the lowest value among all of the compared methods. In terms of the true-positive rate, which indicates the undersegmentation rate, p-ESRAC produced a lower value (**92.5** $\pm$ 3.1%) than the other methods (p-CVRAC, 99.2 $\pm$ 1.1%; p-GAR, 98.4 $\pm$ 2.5%; LRAC, 94.8 $\pm$ 8.5%) because the gradient close to the boundaries was strong, which increased the risk of undersegmentation near the border. However, this issue is not serious because the voxels of the sub-border are of little interest in subsequent image analysis. p-ESRAC had the lowest values for the average symmetric surface distance. Based on the R^2 in Fig. 9, the volume was most linearly correlated between the automatic and manual segmentations for LRAC and p-ESRAC. Additionally, note that LRAC achieved good segmentation quality, similar to that of p-ESRAC, for most of the metrics.

For the malignant cases, p-ESRAC achieved slightly lower accuracy than that for the normal cases, yet it still outperformed the other techniques—the mean dice similarity coefficient was 91.6% in the malignant cases compared to 93.9% in the normal cases, the mean false-positive rate was 7.9% (malignant) compared to 4.5% (normal), and the average symmetric surface distance was 2.5 mm (malignant) compared to 1.8 mm (normal). These results occurred because the liver in the malignant cases was seriously damaged, leading to loss of liver function such that the contrast in the liver was poor. Additionally, this liver damage was accompanied by anatomical changes. However, the test results in both cases demonstrated that LRAC was not relatively robust—the mean dice similarity coefficient was 61.5% (malignant) compared to 90.8% (normal), the mean false-positive rate was 94.5% (malignant) compared to 14.0% (normal), and the average symmetric surface distance was 7.2 mm (malignant) compared to 2.7 mm (normal). We measured the ratio of the missing structures, such as vasculature or outstanding textural features in the liver, which were not captured by active contours but were included by additional iterative morphological operations. Compared with p-GAR and LRAC, as shown in Table III, the ratio of p-ESRAC was higher by a factor of approximately 2 (11.78 $\pm$ 1.09%) compared to its counterparts because of the greater sensitivity of the edge map to

the regional information. Figure 10 illustrates how well p-ESRAC responded to the edges around the structures in the liver. This characteristic might be undesirable for segmenting the entire liver volume. However, if only the parenchymal region is considered for computer-aided diagnosis, and extra vessel segmentation is bypassed, p-ESRAC would be the best choice among them. Even for whole-liver segmentation, an iterative morphological iteration step is necessary, not only in p-ESRAC but also in its counterparts. Thus, it is difficult to claim that the greater response of p-ESRAC to hepatic structures constitutes some vulnerability in its application.

4. DISCUSSION

The main objectives of this paper were to introduce a novel hybrid active-contour framework for liver segmentation and to compare its performance to that of other existing active contours in multiphase contrast-enhanced liver MRI. Segmentation of the liver is an extremely difficult, complex task because of dual enhancement and the geometric proximity to other tissues adjacent to the liver, including the right kidney. To address these problems, we presented a novel edge-function-scaled (weighted) region-based active contour algorithm and utilized multiphase contrast-enhanced image sequences to address the leakage-to-kidney and under- and over-segmentation problems. We applied the multiple-partition scheme to the active-contour framework because of the inhomogeneous intensity distribution, and we verified this application through qualitative and quantitative evaluations with manually segmented reference volumes from 14 normal or benign cases and 16 cases with malignant liver lesions. The experimental results revealed that the ESRAC model markedly reduced oversegmentation, including leakage to the kidney, which was the main strength of this model. Furthermore, its partitioned version, p-ESRAC, at an optimized angular distance of 45°, increased the true segmentation by 5.4% over ESRAC for benign cases and 22.2% for malignant cases. In comparison to other intensity-based segmentation methods (p-CVRAC, GAC, p-GAR, and LRAC), p-ESRAC yielded
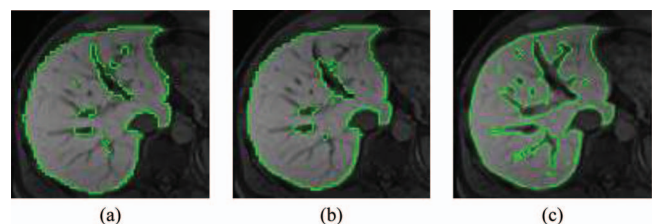

FIG. 10. Response of (a) p-GAR, (b) LRAC, and (c) p-ESRAC to high gradients before applying iterative morphological iterations.

the most accurate performance; it exhibited a mean dice similarity coefficient of $93.9 \pm 1.6\%$ for normal or benign cases and $91.6 \pm 2.2\%$ for malignant cases, demonstrating robust performance in both sets of patients. A limitation of p-ESRAC is that it is more likely to exclude internal structures, such as vasculature and strong texture features, in segmentation than the other techniques. The reason for this behavior is the high responsiveness of this model to the edge map. However, overall, intensity-based active contours are also not entirely free from this issue, so they must generally undergo postprocessing, such as morphological operations, to include the internal structures. Additionally, because multiphase image data were used in our model, image registration was an essential prerequisite.

In this study, we used an Intel Xeon CPU X5355 @ 2.66 GHz with 16 GB of main memory in a Linux OS. The overall process of evaluating the p-ESRAC model included detecting the inferior vena cava, initializing seeds, resampling, downsampling, and implementing the active contour and IMO. Completing all of the computations took 13 min, including 1 min for registration using GPU processing, 7.8 min of which were required for implementing the active contour for 700 iterations to resampled and downsampled images. In contrast, manual segmentation required approximately 30 min for one subject. Therefore, by employing the automated p-ESRAC model, the segmentation time was reduced by 57%. The other active contours required similar computation times to p-ESRAC except for LRAC, which took 3–5 times longer, which is one of the disadvantages of LRAC.

5. CONCLUSION

We developed a hybrid active contour model for segmentation of the liver on contrast-enhanced liver MRI. This model was designed to prevent oversegmentation and leakage to adjacent organs, particularly the right kidney, and it was achieved by weighting regional information with an edge map computed from a combination of the registered arterial and delayed phases, coupled with a geodesic edge term. A partition scheme was applied to the model to increase the true-positive segmentation rate. Experiments on 30 patient subjects, consisting of 14 normal or benign cases and 16 malignant cases, showed that our model outperformed the other existing active contours. Therefore, p-ESRAC is a promising segmentation technique for DCE liver MRI. In future work, we will verify our algorithm in other applications and target and translate the use of this algorithm to clinics.

ACKNOWLEDGMENTS

a)Author to whom correspondence should be addressed. Electronic mail: xhu3@emory.edu

[1]Y. Boykov and G. Funka-Lea, "Graph cuts and efficient N-D image segmentation," Int. J. Comput. Vis. **70**, 109–131 (2006).

[2]E. N. Mortensen and W. A. Barrett, "Intelligent scissors for image composition," in *Proceedings of the 22nd Annual Conference on Computer Graphics and Interactive Techniques – SIGGRAPH '95, Los Angeles, CA, 1995* (ACM, New York, 1995), pp. 191–198.

[3]U. Vovk, F. Pernus, and B. Likar, "A review of methods for correction of intensity inhomogeneity in MRI," IEEE Trans. Med. Imaging **26**, 405–421 (2007).

[4]T. Heimann *et al.*, "Comparison and evaluation of methods for liver segmentation from CT datasets," IEEE Trans. Med. Imaging **28**, 1251–1265 (2009).

[5]K. A. Saddi and C. Chefd, "Global-to-local shape matching for liver segmentation in CT imaging," in *Proceedings of the MICCAI, Brisbane, Australia, October 2007* (Springer, New York, 2007), pp. 207–214.

[6]D. Kainm, T. Lange, and H. Lamecker, "Shape constrained automatic segmentation of the liver based on a heuristic intensity model," in *Proceedings of the MICCAI Workshop on 3D Segmentation in the Clinic: A Grand Challenge, Brisbane, Australia, 2007* (Springer, New York, 2007), pp. 109–116.

[7]P. Slagmolen *et al.*, "Atlas based liver segmentation using nonrigid registration with a B-spline transformation model," in *Proceedings of MICCAI Workshop on 3D Segmentation in the Clinic: A Grand Challenge, Brisbane, Australia, 2007* (Springer, New York, 2007), pp. 197–206.

[8]D. Furukawa, A. Shimizu, and H. Kobatake, "Automatic liver segmentation method based on maximum a posterior probability estimation," *3D Segmentation in the Clinic: A Grand Challenge* (Springer, New York, 2007), pp. 117–124.

[9]L. Ruskó and G. Bekes, "Liver segmentation for contrast-enhanced MR images using partitioned probabilistic model," Int. J. Comput. Assist. Radiol. Surg. **6**, 13–20 (2011).

[10]N. Paragiosl and R. Deriche, "Coupled geodesic active regions for image segmentation: A level set approach," Computer Vision — ECCV 2000, Dublin, Ireland, Vol. 1843 (Springer, New York), pp. 224–240.

[11]S. Lankton and A. Tannenbaum, "Localizing region-based active contours," IEEE Trans. Image Process. **17**, 2029–2039 (2008).

[12]S. Lankton, D. Nain, A. Yezzi, and A. Tannenbaum, "Hybrid geodesic region-based curve evolutions for image segmentation," Proc. SPIE **6510**, 65104U (2007).

[13]J. Oh, D. Martin, and O. Skrinjar, "GPU-based motion correction of contrast-enhanced liver MRI scans: An OpenCL implementation," in *Proceedings of the IEEE International Symposium on Biomedical Imaging From Nano to Macro, Chicago, New York, 2011* (IEEE, Chicago, New York, 2011), pp. 783–786.

[14]M. Styner, C. Brechbühler, G. Székely, and G. Gerig, "Parametric estimate of intensity inhomogeneities applied to MRI," IEEE Trans. Med. Imaging **19**, 153–165 (2000).

[15]J. V. Manjón *et al.*, "A nonparametric MRI inhomogeneity correction method," Med. Image Anal. **11**, 336–345 (2007).

[16]C. Sc, "Generalizing the Hough transform to detect arbitrary shapes," Pattern Recognition **11**, 111–122 (1981).

[17]Y. Xie and Q. Ji, "A new efficient ellipse detection method," in *Proceedings of the 16th International Conference on Pattern Recognition, 2002* (IEEE, New York, 2002), pp. 957–960.

[18]F. Sutherland and J. Harris, "Claude Couinaud: a passion for the liver," Arch Surg. **137**(11), 1305–1310 (2002).

[19]R. D. Martin, R. Danrad, and S. M. Hussain, "MR imaging of the liver," Radiol. Clin. North Am. **43**, 861–886 (2005).

[20]K. I. Ringe, D. B. Husarik, C. B. Sirlin, and E. M. Merkle, "Gadoxetate disodium-enhanced MRI of the liver: Part 1, protocol optimization and lesion appearance in the noncirrhotic liver," AJR Am. J. Roentgenol. **195**, 13–28 (2010).